

Large Eddy Simulations of Double-Ruler Electromagnetic Field Effect on Transient Flow During Continuous Casting

RAMNIK SINGH, BRIAN G. THOMAS, and SURYA P. VANKA

Transient flow during nominally steady conditions is responsible for many intermittent defects during the continuous casting of steel. The double-ruler electromagnetic field configuration, or “FC-Mold EMBr,” is popular in commercial slab casting as it provides independent control of the applied static field near the jet and free surface regions of the mold. In the current study, transient flow in a typical commercial caster is simulated in the absence and in the presence of a double-ruler magnetic field, with rulers of equal strengths. Large eddy simulations with the in-house code CU-FLOW resolve the important transient behavior, using grids of over five million cells with a fast parallel solver. In the absence of a magnetic field, a double-roll pattern is observed, with transient unbalanced behavior, high surface velocities (~ 0.5 m/s), surface vortex formation, and very large surface-level fluctuations ($\sim \pm 12$ mm). Applying the magnetic field suppresses the unbalanced behavior, producing a more complex mold flow pattern, but with much lower surface velocities (~ 0.1 m/s), and a flat surface level with small level fluctuations ($< \pm 1$ mm). Nail board measurements taken at this commercial caster, in the absence of the field, matched reasonably well with the calculated results, both quantitatively and qualitatively.

DOI: 10.1007/s11663-014-0022-2

© The Minerals, Metals & Materials Society and ASM International 2014

I. INTRODUCTION

THE quality of steel products is greatly affected by the fluid flow near the top surface of the mold during the continuous casting process. Maintaining stable flow conditions is well known to produce steel of the best quality. The flow pattern depends on the nozzle geometry, casting speed, mold width, mold thickness, argon gas injection, and submergence depth. In conventional slab casting, if the jet impinges first on the free surface, a “single-roll” flow pattern is generated. If the jet first impinges on the narrow face, and splits, flowing up toward the free surface, then a “double-roll” flow pattern is generated. When the control parameters create conditions which fall on the borderline between single and double rolls, then complex unstable flow conditions are likely. The highly turbulent nature of flow in the mold causes transient behavior even during statistically steady-state operation. Sudden increases in velocity, level fluctuations, vortex formation, and other intermittent flow events can lead to the entrainment of mold slag, the formation of surface defects, and other quality problems. One of the few process parameters that potentially could be adjusted to respond to changes in the flow is the application of electromagnetic fields. In

addition, the electromagnetic forces change naturally in response to changes in the instantaneous, local turbulent flow.

In steel slab casting, both static and moving magnetic fields have been implemented. Statically-applied electromagnetic-field (EMF) configurations include local [circular fields on each side of the Submerged Entry Nozzle (SEN)],^[1–5] single-ruler (a rectangular field across the entire mold width),^[5,6] and double-ruler^[6–9] (two ruler-shaped fields, with one positioned across the mold near the meniscus and the other one aligned through or below the nozzle ports). When the EMF coil currents are adjusted to produce equal peak field strengths, this double-ruler configuration is commercially known as “Flow-Control-Mold” or “FC-Mold” ElectroMagnetic Braking or “EMBr.” The regions of the strongest magnetic fields tend to deflect the flowing steel, altering the time-averaged flow, which has been the subject of many previous modeling studies.^[1,3,4,6,10–13] The effect on transient flow has received less attention in the studies so far.

The flow of a conducting fluid such as steel through a magnetic field generates a force opposing the motion, and thus should be self-stabilizing. However, the magnetic field can change the flow stability in non-obvious ways.^[6] Previous study has shown that conducting walls, such as the solid steel shell surrounding the liquid cavity in continuous casting, have a stabilizing effect on the flow. For example, large eddy simulations (LES) and Ultrasonic Doppler Velocimetry (UDV) measurements of mold flow in a scaled physical model with GaInSn, a low melting liquid metal alloy, were performed to study the effects of ruler EMBr on transient flow phenomena, with conducting (brass) vs insulated (plastic) side

RAMNIK SINGH, MS Student, BRIAN G. THOMAS and SURYA P. VANKA, Professors, are with the Department of Mechanical Science and Engineering, University of Illinois at Urbana-Champaign, Urbana IL, 61801. Contact e-mail: bgthomas@illinois.edu.

Manuscript submitted September 21, 2013.

Article published online January 25, 2014.

walls.^[12,13] The application of a single-ruler EMBr over the nozzle with the insulated walls made the mold flow unstable, with a large-scale wobbling of the jets. With insulating walls, the current loops returning through the molten steel induce forces which deflect the local current-carrying flow, thus carrying forward the flow-stabilizing effects to locations elsewhere through a complex feedback manner. This behavior is suppressed with conducting side walls, such as the solidifying steel shell of a real caster. This is because the forces induced by current loops returning through the solid shell have no effect.

In the current study, we perform two LES of the mold flow in a real commercial caster to investigate the effect of an applied double-ruler EMBr magnetic field configuration. The transient and the time-averaged results of the two simulations performed in the presence and in the absence of electromagnetics are compared, focussing on surface flow phenomena. Nail board measurements were also taken at the commercial caster and are compared with the calculated results. The commercial caster had no EMBr system, and hence, measurements are only compared with the simulations in the absence of electromagnetics.

II. COMPUTATIONAL MODEL DESCRIPTION

A. Governing Equations for LES of Magnetohydrodynamic (MHD) Flow

In the current study, we solve the unsteady three-dimensional continuity and momentum equations given by Eqs. [1] and [2], respectively.

$$\frac{\partial u_j}{\partial x_j} = 0 \quad [1]$$

$$\begin{aligned} \frac{\partial u_i}{\partial t} + \frac{\partial u_i u_j}{\partial x_j} = & -\frac{1}{\rho} \frac{\partial p^*}{\partial x_i} + \frac{\partial}{\partial x_j} \left((v + v_s) \left(\frac{\partial u_i}{\partial x_j} + \frac{\partial u_j}{\partial x_i} \right) \right) \\ & + \frac{1}{\rho} F_i \quad i = 1, 2, 3, \end{aligned} \quad [2]$$

where i, j imply the tensor notation, and repeated indices in a term indicate summation; u_i are the three velocity components; p^* is the pressure modified to include the filtered normal stresses ($p^* = p + (1/3)\rho\tau_{kk}$), where p is the static pressure; ρ is the fluid density; v is the kinematic viscosity; and F_i in Eq. [1] represents the three Lorentz-force components. The effects of the flow

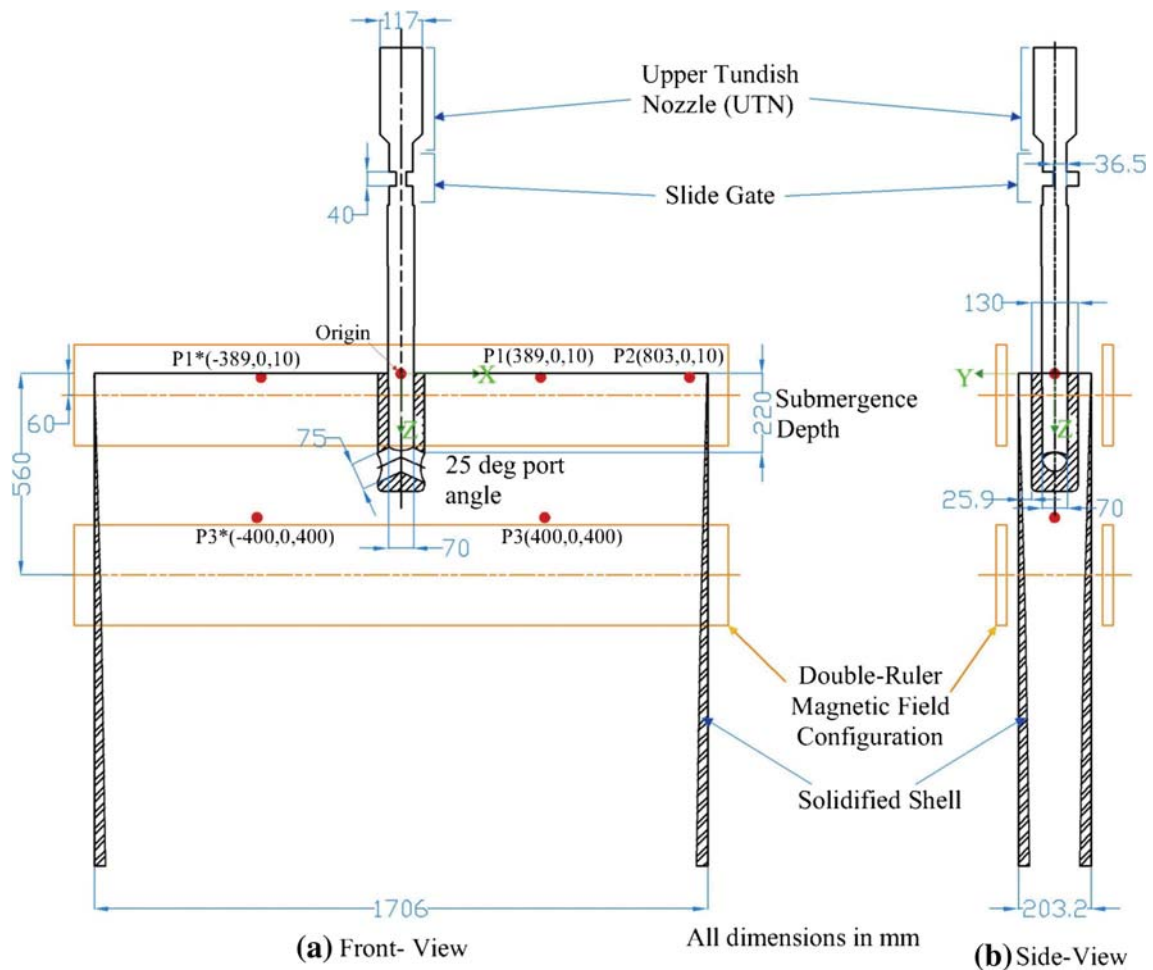


Fig. 1—Geometry of the commercial caster with two rectangles showing the location of the double-ruler EMBr field.

Table I. Process Parameters (Real Commercial Caster)

Mold width (L)	1706.0 mm
Mold thickness	203.2 mm
Mold/strand length in computational domain	3600.0 mm
Nozzle port diameter	75.0 mm
Nozzle bore diameter (d) (inner outer)	70 mm 130 mm
Nozzle port angle	25.0 deg
Slide gate orientation	90.0 deg
Slide gate opening fraction (f_A)	41.48 pct
SEN submergence depth (liquid surface to top of port)	220 mm
Total volume flow rate	8.1 L/s
Mass flow rate	3.4 tonne/min
Bulk velocity at UTN inlet	0.752 m/s
Bulk velocity in SEN cross section (U)	2.1 m/s
Casting speed	1.4 m/min
Argon gas injection (volume fraction)	4.37 pct (ignored)
Thickness of shell (uniform around perimeter)	s (mm) = $2.75\sqrt{t(s)}$
Kinematic viscosity (steel)	$0.86 \times 10^{-6} \text{ m}^2/\text{s}$
Fluid density (steel)	7000 kg/m^3
Conductivity of liquid (σ_{liquid})	$0.714 \times 10^6 \text{ 1}/\Omega\text{m}$
Conductivity of solid-steel-shell walls (σ_{wall})	$0.787 \times 10^6 \text{ 1}/\Omega\text{m}$
Reynolds number ($Re = Ud_{\text{inner}}/\nu$, based on nozzle diameter)	171000
Reynolds number ($Re = UL/\nu$, based on mold width)	4166000
Hartmann number ($Ha = BL\sqrt{\sigma/\rho\nu}$, based on mold width)	5200
Froude number ($Fr = U/\sqrt{gL}$, based on mold width)	0.513
Stuart number ($N = B_0^2 L \sigma / \rho U$, based on mold width)	6.5
Cases	1. No-EMBr 2. With EMBr

phenomena too small to be captured by the grid spacing, and thus spatially filtered, are incorporated by an eddy viscosity ν_s which is modeled with the Coherent-structure Smagorinsky Model (CSM) Sub-Grid Scale (SGS) model.^[14]

The molten steel flowing through the magnetic field generates an electric current \vec{J} , which flows through the entire domain to produce the Lorentz force \vec{F} , and is given by

$$\vec{J} = \sigma(\vec{E} + \vec{u} \times \vec{B}_0) = \sigma(-\nabla\phi + \vec{u} \times \vec{B}_0) \quad [3]$$

This equation neglects the induced magnetic field, which is small compared with the applied magnetic field in this system.^[1,15] The charge conservation condition, $\nabla \cdot \vec{J} = 0$, is then used to find the potential ϕ .

$$\nabla \cdot (\sigma \nabla \phi) = \nabla \cdot (\sigma(\vec{u} \times \vec{B}_0)) \quad [4]$$

The Lorentz force \vec{F} is given by

$$\vec{F} = \vec{J} \times \vec{B}_0, \quad [5]$$

where σ is electrical conductivity; \vec{E} is the induced electric field, ϕ is electric potential; and \vec{B}_0 is the applied magnetic field, which can be measured in the absence of flowing metal.^[8]

This set of coupled MHD equations (Eqs. [1]–[5]) is solved by the finite volume method and implemented on a graphics processing unit (GPU) for fast computation in the in-house code CUFLOW. The numerical details

of solving these equations with CUFLOW have been discussed in previous studies,^[16–19] and hence, are only briefly described in Section II–F.

B. Computational Domain

The complete geometry of the commercial caster, including the Upper Tundish Nozzle (UTN), the slide gate, the SEN with bifurcated round ports, and the mold, is given in Figure 1 and Table I. The computational domain for the current study included both the liquid region, shown in Figure 2, and a separate region consisting of the solidifying shell, which was initialized to move with the casting speed (Table I) in the casting direction. The slide gate, which moves perpendicular to the wide face (WF), is used as the flow control mechanism in the commercial caster. The position of the slide gate was 41.48 pct open (36.5-mm opening), which was calculated according to the liquid steel throughput rate, nozzle geometry, tundish height, and argon gas injection rate using a model, based on Bernoulli's equation and empirical relations, developed by Liu and Thomas.^[20]

C. Solidifying Shell Profile

The fluid flow in the mold has relatively little effect on the shape of the shell. The shell profile is controlled by the heat transfer rate through the interfacial gap to the mold wall, and the casting speed. Thus, although the shell profile has some influence on the fluid flow, it is not

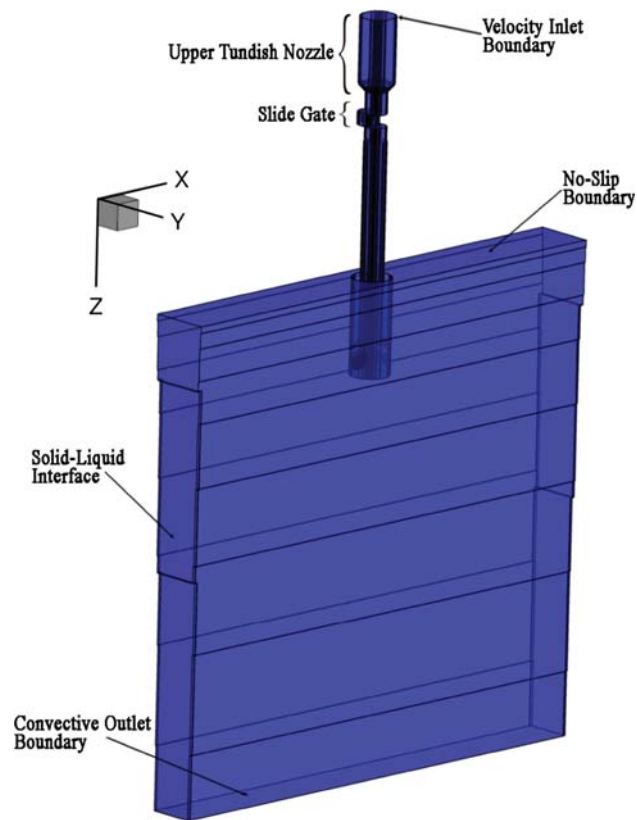


Fig. 2—Isometric view of the computational domain (fluid flow region) with boundary conditions.

changed much by the fluid flow. Therefore, a steady approximation of the solidifying shell profile is applied in the current study, which requires no iterations to improve the shell profile. The shell thickness s at any given location below the meniscus was calculated from

$$s = k\sqrt{t}, \quad [6]$$

where t is the time (s) taken by the shell to travel the given distance from the meniscus at the casting speed, and the constant k ($= 2.75 \text{ mm}/\sqrt{\text{s}}$) was chosen to match the steady-state shell thickness profile (mm) based on break-out shell measurements by Iwasaki *et al.*^[21] for a similar caster.

D. Electromagnetic Field

A double-ruler EMBr configuration was applied with the maximum strength of the upper-ruler and lower-ruler fields occurring at 60 and 560 mm below the free surface, respectively. Figure 3 shows a contour plot of the applied magnetic field and Figure 4 shows its variation in the casting direction. The magnetic field applied here is adopted from a study by Idogawa *et al.*^[8] on the effect of this EMBr configuration using experiments with a scaled mercury model, numerical simulations using a Reynolds Averaged Navier–Stokes (RANS) model, and experiments in a real caster. The field is assumed to be uniform in the width and thickness

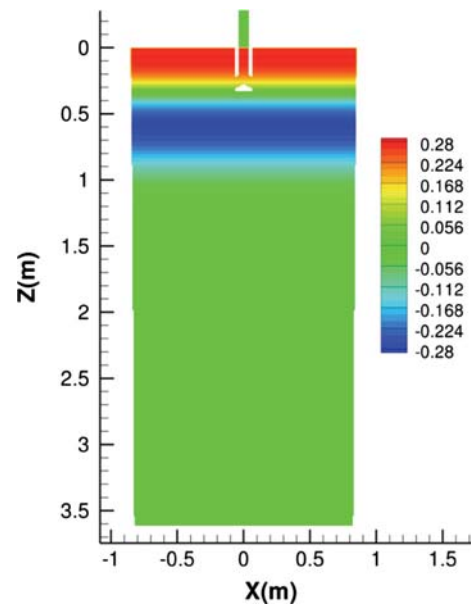


Fig. 3—Contour plot of the applied magnetic field.

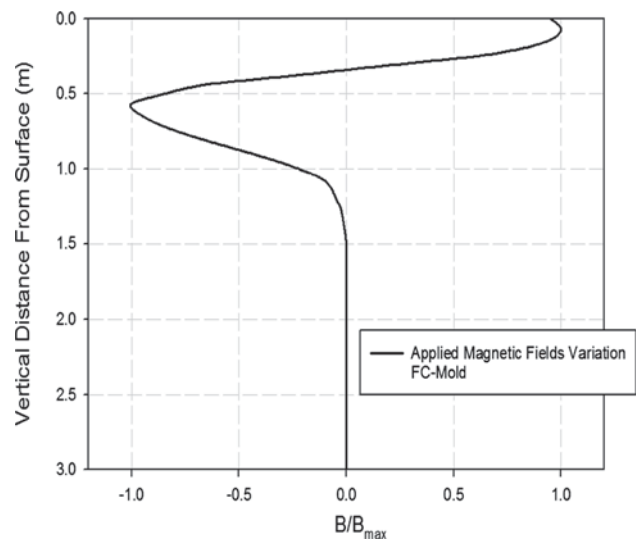


Fig. 4—Variation of applied magnetic field in the casting direction (Z) with $B_{\text{max}} = 0.28 \text{ T}$ in the EMBr case.

directions of the caster. Both rulers have only one non-zero magnetic field component, which acts in the Y-direction.

E. Mesh and Boundary Conditions

A Cartesian mesh was used in the current study with 5.5 million finite volume cells. To generate the caster geometry, first a rectangular domain was meshed with 8.9 million cells. Then, solid regions were blocked out. A uniform fixed-velocity boundary condition of 0.752 m/s was applied at the inlet at the top of the UTN, based on the casting speed and the UTN inlet area. A no-slip boundary condition was applied on the

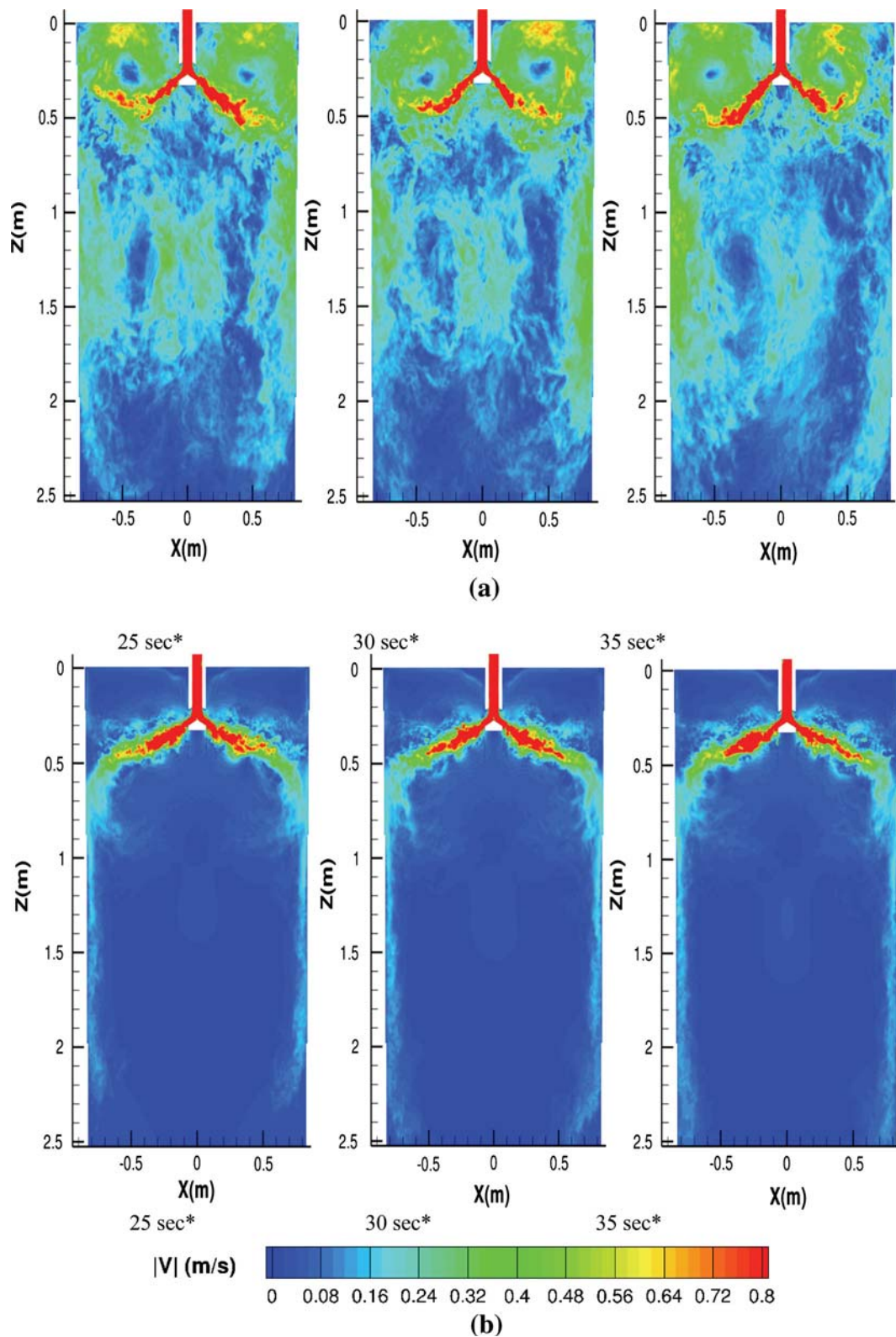


Fig. 5—Contour plots of instantaneous velocity magnitude for (a) No-EMBr case and (b) EMBR case (*Time from start of simulation).

free surface of the mold to approximately model the effects of the high viscosity slag on slowing down the steel/slag interface.^[22] A convective

boundary condition was applied to the outlet of the caster for all three velocity components according to Eq. [7].

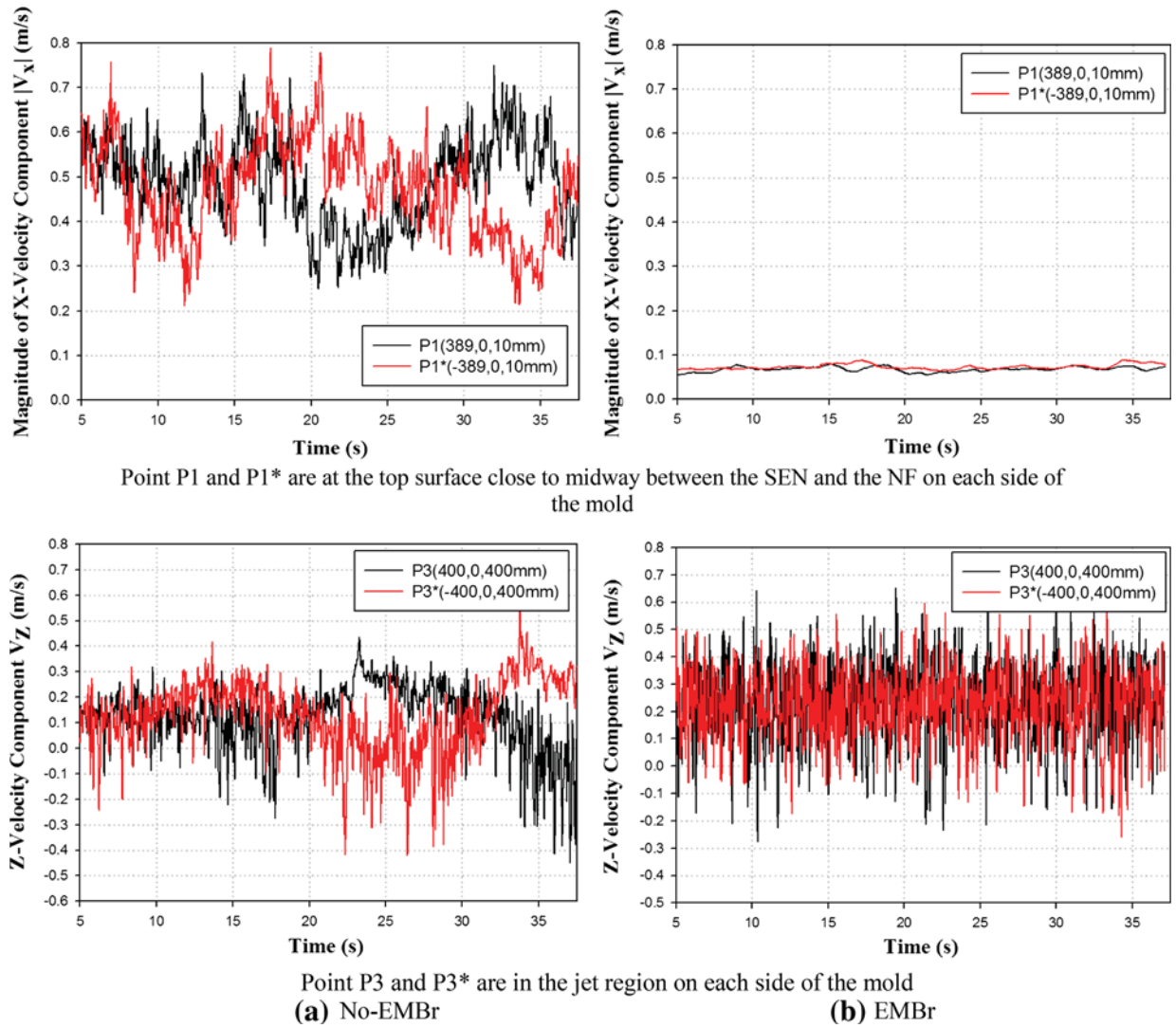


Fig. 6—Time histories of velocity components showing unbalanced flow at mirror-imaged locations in the SEN centerline (P1 near surface and P3 in jet shown in Fig. 1) for (a) No-EMBr case and (b) EMBR case.

$$\frac{\partial u_i}{\partial t} + U_{\text{convective}} \frac{\partial u_i}{\partial n} = 0 \quad i = 1, 2, 3, \quad [7]$$

where $U_{\text{convective}}$ is the average normal velocity across the outlet plane, and n is the direction normal to the outlet plane. The solidifying shell was given fixed downward vertical velocity at the casting speed, which causes the liquid to leave the liquid domain to account for both the mass transfer and the momentum transfer from the fluid region to the solidifying shell. All other boundaries were treated as solid walls with the wall-function model of Werner and Wengle.^[23] The fluid flow equations were solved only in the fluid domain, and the MHD equations were solved in the entire computational domain, including the solid shell. An insulated electrical boundary condition ($\frac{\partial \phi}{\partial n} = 0$) was applied to the outermost boundary of the computational domain to simulate the nonconducting mold slag layer that surrounds the solid shell.

F. Numerical Method and Computational Cost

CUFLOW solves the coupled MHD equations on a structured Cartesian grid using a NVIDIA Tesla C2075 GPU. This code uses a fractional step method for the pressure–velocity coupling and the Adams–Bashforth temporal scheme and second order finite volume method for discretizing the momentum equations. The pressure Poisson equation (PPE) and the electric Poisson equation (EPE) (Eq. [4]) are solved using a geometric multigrid solver.

Simulations for both cases, No-EMBr and EMBR, were started from a zero initial velocity. The flowfields were allowed to develop for 10 seconds (200,000 time steps) and 20 seconds (400,000 time steps) for the No-EMBr and EMBR cases, respectively, before collecting the time-averages. Time-averages were stabilized for 5 seconds in both cases, and then turbulence statistics were collected for 20 and 15 seconds for the No-EMBr and EMBR cases, respectively. The computational

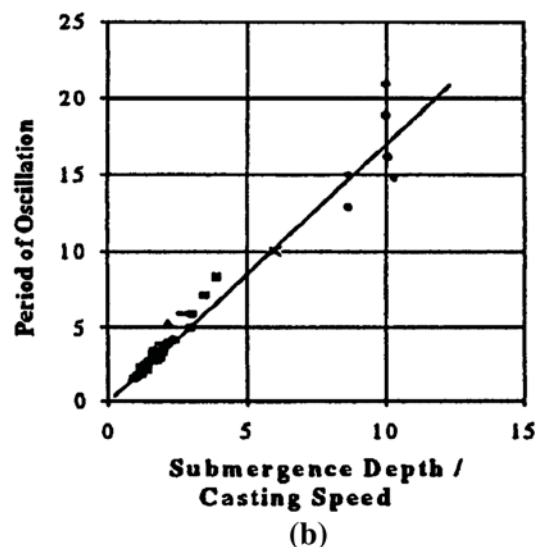
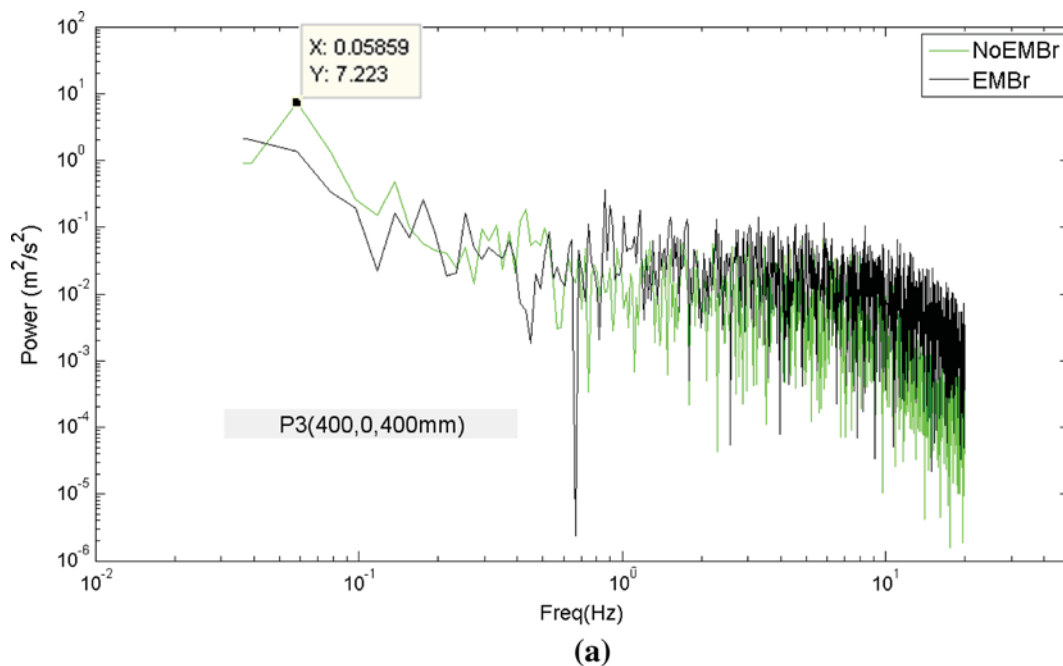


Fig. 7—(a) Power spectrum of V_z at P3 in the jet region. (b) Measured Period of oscillation plotted against ratios of submergence depths and casting speeds from water models and real caster.^[28]

expense of the EMBR case was nearly twice that of the No-EMBr case, as the former requires the solution of the EPE. The 35 seconds of simulation in the absence of the magnetic field required a total of 15 days of calendar computation time, whereas the 40 seconds of simulation with the magnetic field consumed 34 days.

III. TRANSIENT RESULTS

A. Mold Flow

The conditions for this caster (Table I) produce a typical “double-roll” flow pattern in the mold for both the cases simulated, with strong flow across the top surface from the narrow face toward the SEN, and a lower roll that penetrates deep into the strand. Fig-

ure 5(a) shows instantaneous contours of velocity magnitude in the mold region with no EMBR. Comparing these instantaneous snapshots clearly shows unbalanced flow, with transient asymmetries that alternate between the two halves of the mold. This unbalanced flow is not due to any geometric asymmetry. Displacement of the slide gate parallel to the WFs would produce consistently asymmetrical flow, but in this caster, the slide gate is displaced perpendicular to the narrow faces in the more common “90-deg orientation.”^[24,25] This unbalanced flow is likely aggravated by the mountain-bottom (pointed-bottom) shape of this nozzle, which creates strong low-frequency fluctuations, relative to well-bottom nozzles.^[26] The application of the EMBR field suppresses all the scales of turbulence captured in the current study, from small eddies (<1 mm) to large side-

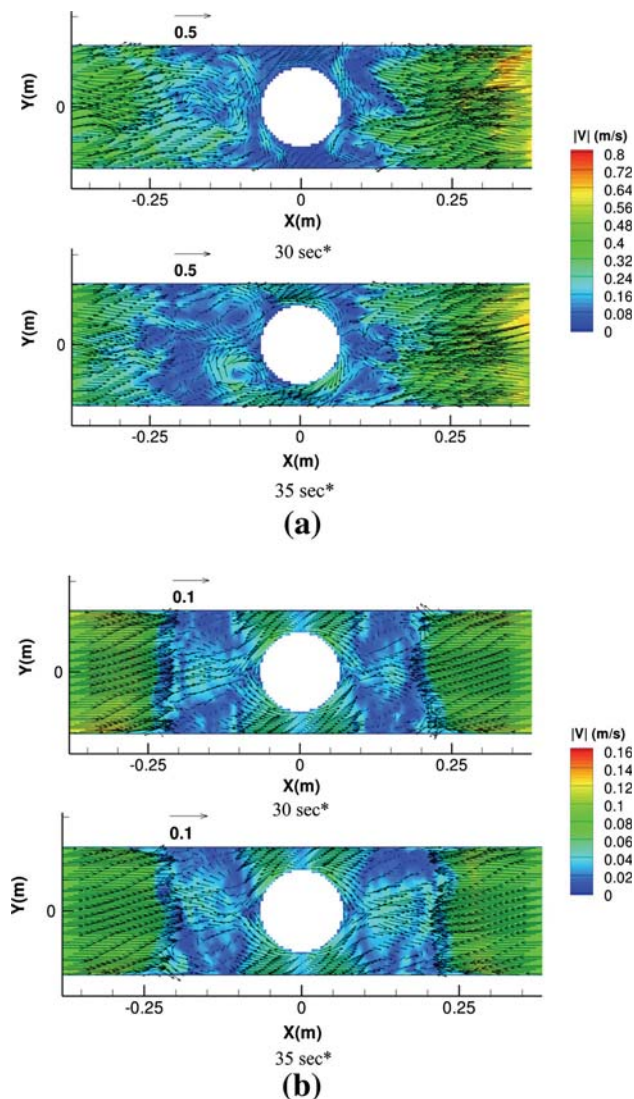


Fig. 8—Contours of velocity magnitude with vectors, of V_x and V_y , 10 mm from the top surface for (a) No-EMBr case, and (b) EMBr case (*Time from start of the simulation, 90 pct of vectors skipped for clarity).

to-side sloshing on the scale of the caster, as seen in Figure 5(b). The jet velocity is dampened, which weakens the flow velocity in both the upper and lower rolls.

To quantify the unbalanced mold flow, Figure 6 compares the time history of velocity components at two points (P1 and P3, shown in Figure 1) and their respective mirror images about the SEN centreline (P1* and P3*) for both the No-EMBr and EMBr cases. Points P1 and P1* are on the surface, midway between SEN and NF, and points P3 and P3* are inside each jet. In the No-EMBr case, at both locations, very strong unbalanced flow behavior develops after ~15 to 20 seconds. The maximum temporal difference in jet velocities is ~0.3 m/s. This evolves into transient unbalanced flow at the surface with differences in surface velocities up to ~0.3 m/s, and frequent reversals in flow direction. In addition, the unbalanced flow has strong spatial variations: sometimes strong surface flow is from right to left,

(6a-top), and sometimes from left to right. This unbalanced flow can be detrimental because it tends to create more top surface fluctuations, vortex formation, upward flow impinging on the top surface, and slag crawling.^[27] Unbalanced flow may also increase the penetration depth of inclusions and bubbles.^[9] The application of the EMBr field damps this unbalanced behavior of mold flow as seen in Figure 6(b) at both locations.

A power spectrum analysis was performed for the transient velocity component V_z at P3 in the jet region, and the distribution of power over the frequency domain is shown in Figure 7(a). The frequency domain is resolved from 0.028 to 20 Hz. The lowest frequency is limited by the total simulation time of 35 seconds (~0.028 Hz) for the No-EMBr case. The highest frequency resolved with Fast Fourier Transform (FFT) is half of the signal sampling rate which was 40 Hz or once after every 500 time steps of the simulation.

Lower frequencies contain more power for both the No-EMBr and EMBr cases. The jets are the source of energy, and they continuously feed the large-scale eddies with the low-frequency fluctuations. The power spectra for the two cases are similar, except for a frequency peak in the No-EMBr case at 0.059 Hz which should correspond to the frequency of the unbalanced flow behavior. Honeyands *et al.*^[28] reported strong mold flow oscillations with a period corresponding to a linear function of the ratios between the submergence depth and casting speed, based on experimental data from water models and real casters as shown in Figure 7(b). The oscillation period for the current real caster (submergence depth/casting speed = 9.43 seconds) predicted by Figure 7(b) is ~16 seconds, which matches closely with the period corresponding to the peak in the spectrum analysis (0.059 Hz or 16.95 seconds). This also confirms that the simulation of 35 seconds for the No-EMBr case with unbalanced behavior is sufficient to capture these flow transients. In the EMBr case, flow is more stable, with no strong peak at 0.059 Hz. Thus, its transients can be captured with even less simulation time.

B. Top Surface Behavior

Flow past bluff bodies results in vortex shedding which forms a Kármán vortex street. This phenomenon may occur near the SEN if an unbalanced flow between sides of the mold is observed in the top surface.^[29,30] If accompanied by downward flow, then these vortices at the surface can entrain a funnel of molten slag into the molten steel. However, the creation of these slag funnels does not necessarily result in entrainment of slag particles. If the height of the funnel is large enough to reach the jet region, the funnel is broken apart into droplets which are entrained into the jet, leading to slag entrapment in the product.^[30,31] In a double-roll flow pattern, the flow down the SEN combined with vortices caused by any unbalanced surface flow, can lead to entrainment of liquid-slag funnels.^[32,33]

Figure 7 shows four instantaneous snapshots of the contours of velocity magnitude with vectors on the

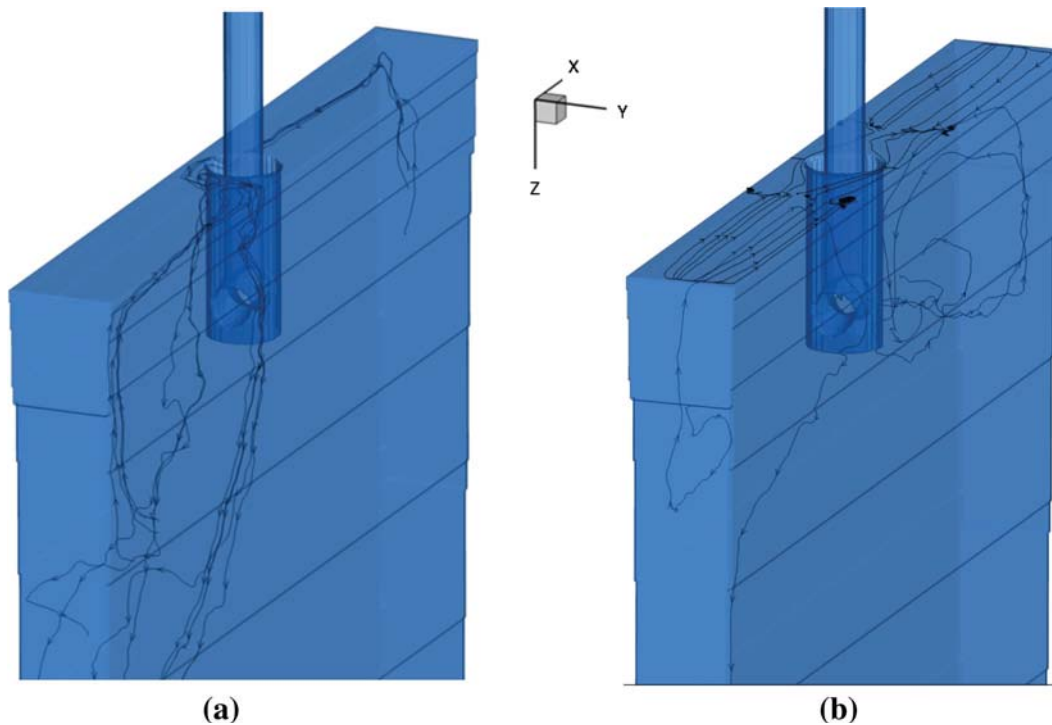


Fig. 9—Streaklines of velocity for the (a) No-EMBr case and (b) EMBr case.

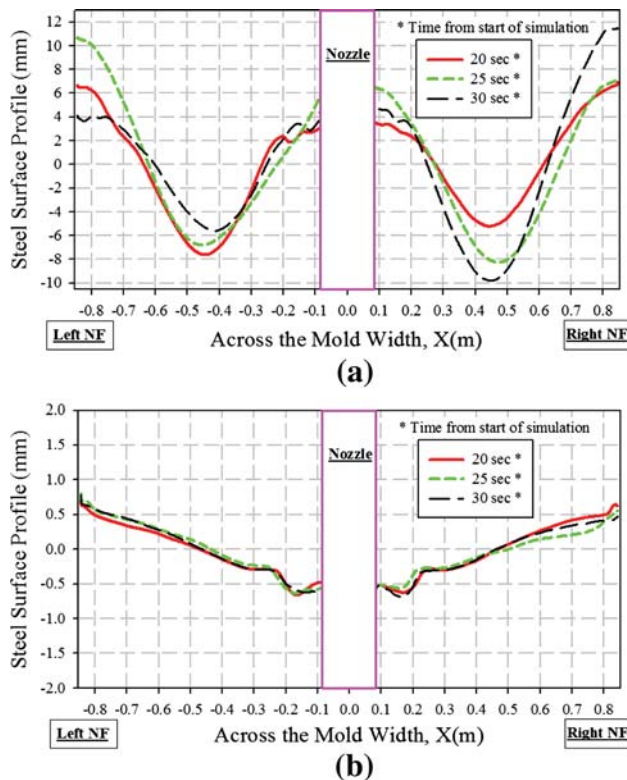


Fig. 10—Surface-level profiles at three instances for (a) No-EMBr case and (b) EMBr case.

surface for both cases. The unbalanced surface flow from the right side in the No-EMBr case can be seen in the two snapshots,. This biased flow across the SEN

leads to vortex shedding, with two strong vortices on the left of the SEN, as seen in the No-EMBr snapshot at 35 seconds. This pair of vortices persisted for ~3 to 4 seconds. The instantaneous plots for the EMBr case indicate no unbalanced flow. The surface velocities are smaller with EMBr (Note: Contour scale range and vector lengths are scaled five times larger with EMBr in Figure 8) and show minimal fluctuations. The flow is mostly directed from the NF to the SEN, except when close to the SEN, where small recirculation regions form.

To visualize the paths of tracer particles in vortices and molten-slag funnels, instantaneous streaklines were plotted in Figure 9 at 35 seconds after the start of the simulation. With No-EMBr, these streaklines show how particles are indeed drawn across the surface from the right past the SEN into rotating vortices near the left of the SEN, and are sucked downward to become entrained into the swirling jet region. In contrast, with EMBr, the streaklines exhibit the simple recirculating flow behavior typical of a double-roll flow pattern. These results show that the No-EMBr case is more susceptible to the formation of the molten-slag funnels, and may likely experience more slag entrainment as a consequence.

Another mechanism for defect formation in the mold is due to the instability of the shape of the top free surface, sometimes called the “standing wave.”^[27] This standing wave is created by flow beneath the free surface and may become unstable if the local slope becomes too high.^[33] In the current study, the surface-level profile is approximated using Eq. [8]^[22] which estimates the liquid surface level by converting the pressure, p , at the top surface into potential energy.

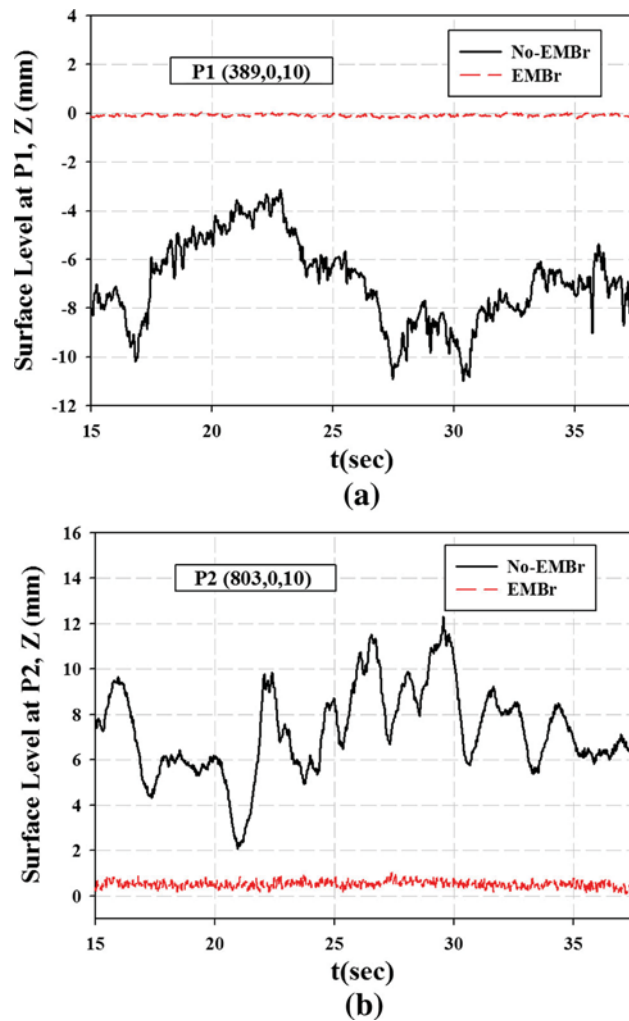


Fig. 11—Time histories of surface-level fluctuations at points close to (a) midway between the narrow face and SEN, P1 (389, 0, 10 mm); and (b) narrow face, P2 (803, 0, 10 mm).

$$Z_{\text{sur}} = \frac{p - p_{\text{mean}}}{\rho_{\text{steel}} g}, \quad [8]$$

where the average pressure p_{mean} was calculated for the line along the top surface at the midplane between the WFs, ρ_{steel} is the steel density, and g is the acceleration due to gravity 9.81 m/s^2 . Figure 10 shows three typical “instantaneous” surface-level profiles, averaged over 1-second time periods separated by 5-second intervals. The No-EMBr case has relatively large variations in surface-level profile across the mold width, with the differences between the peak and the trough ranging from 10 to 21 mm. The highest levels are found near the NF and the SEN, with the level at the NF usually being higher. The high level at the NF is due to the high vertical velocity rising up the NF, whereas the elevated level at the SEN is due to the flow impinging on the SEN outer walls. The application of EMBr flattens the surface level almost completely with a maximum difference between the peak and trough only $\sim 1.5 \text{ mm}$. Another noticeable difference is that in the No-EMBr

case the trough occurs midway between the NF and the SEN, whereas in the EMBr case, the trough occurs close to the SEN outer walls.

Excessive surface-level fluctuation is another detrimental mechanism to steel quality, as it may expose the solidifying dendritic shell to the slag layer, causing entrainment leading to slivers just beneath the surface.^[34] Level fluctuations in the current study were calculated using Eq. [8]. Time histories of level fluctuations are shown in Figure 11 at two typical points, both being 10 mm below the free surface. The first is located close to midway point between the NF and the SEN (P1), and the second is located 50 mm from the NF (P2). At both locations for the No-EMBr case, appreciable turbulent small scales are present and also large scale fluctuations with amplitudes ranging from 5 to 10 mm. Both the small and large scale fluctuations are suppressed by the application of the magnetic field, resulting in stable surface behavior.

IV. TIME-AVERAGED RESULTS

A. Nozzle Flow

Figure 12 compares time-averaged velocities in the SEN regions for both cases. The contour plots look symmetric for both cases, which indicates sufficient averaging time, due to the high velocities in this region. The mountain-bottom SEN produces thin and strong jets,^[26] which are observed in both the cases. Flows inside the SEN ports are similar for both cases because the double-ruler EMBr configuration applies only a low magnetic field in the region around the SEN bottom. The jets exiting the ports have the same downward angle in both cases, although the jet with EMBr is deflected slightly upward as it enters the mold. The applied magnetic field also reduces the velocities in the recirculation region above and below the jet.

To study the flow at the port exits, results of time-averaged velocity magnitude and turbulent kinetic energy (TKE) are shown in Figures 13 and 14, respectively. As expected, these variations are very similar for both the No-EMBr and the EMBr cases as the magnetic field has only a small effect in this region. The velocity magnitude is small at the top of the ports and remains low till midway between the top and bottom walls of the ports, after which it continuously rises reaching its maximum at points close to the bottom of the port exits. The variation of TKE is more complicated. A slightly greater TKE is observed for the EMBr case everywhere along the port exit except close to the top. This is in contrast to our understanding of the applied magnetic field suppressing turbulent fluctuations. However, this phenomenon can be explained by the fact that the flow inside the SEN is initially laminarized by the upper ruler while entering the mold region and then becomes turbulent again as it reaches the nozzle bottom, where the magnetic field is weak.

B. Mold Flow

Figure 15 shows the streamlines and contours of time-averaged velocity magnitude in the mold region for the

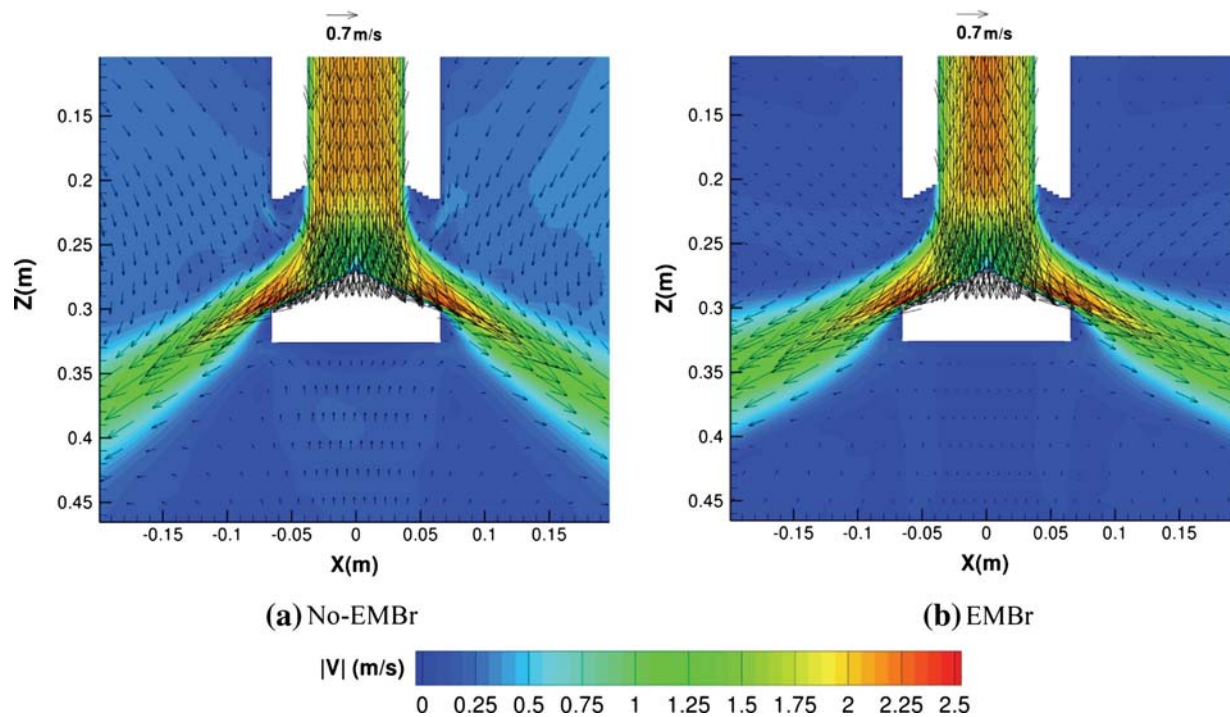


Fig. 12—Contour plots of time-averaged velocity magnitudes with vectors of V_z and V_x in the SEN region for (a) No-EMBr case and (b) EMBr case.

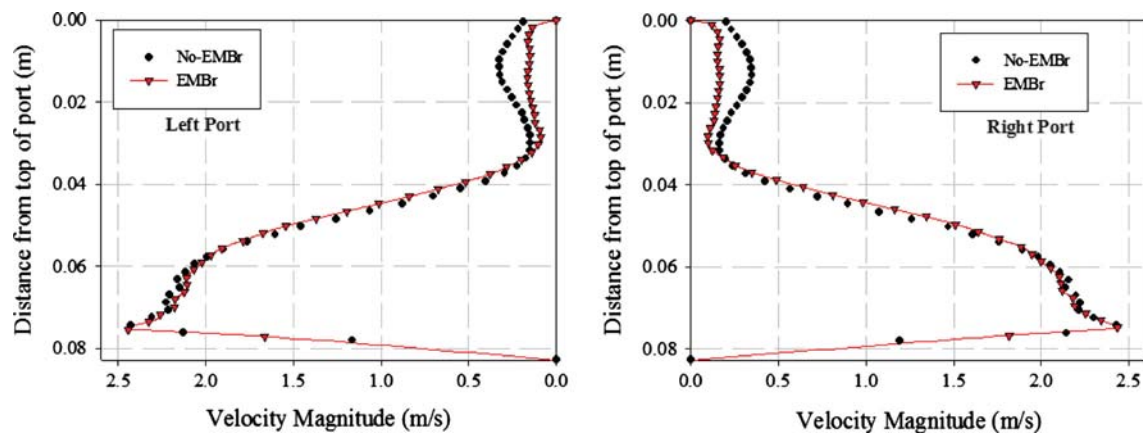


Fig. 13—Variations of time-averaged velocity magnitude along a vertical line, on midplane between WFs, at the port exits.

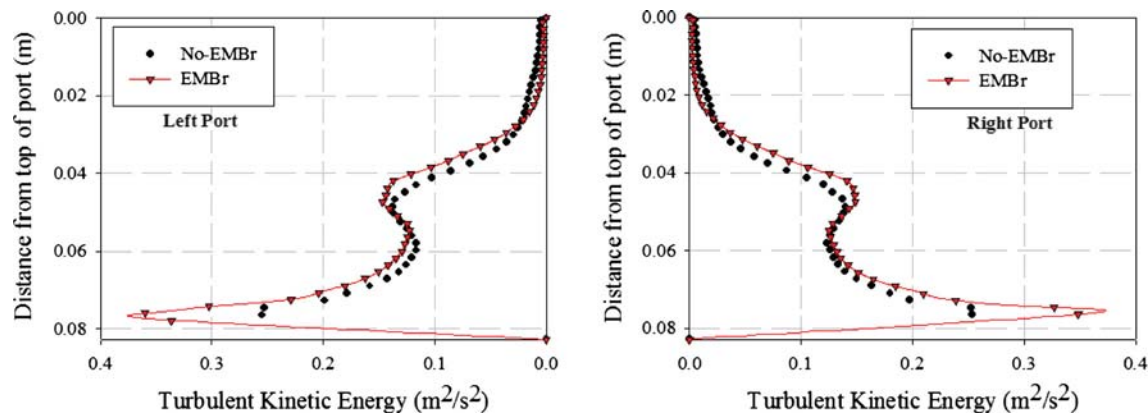


Fig. 14—Variations of TKE along a vertical line, on midplane between WFs, at the port exits.

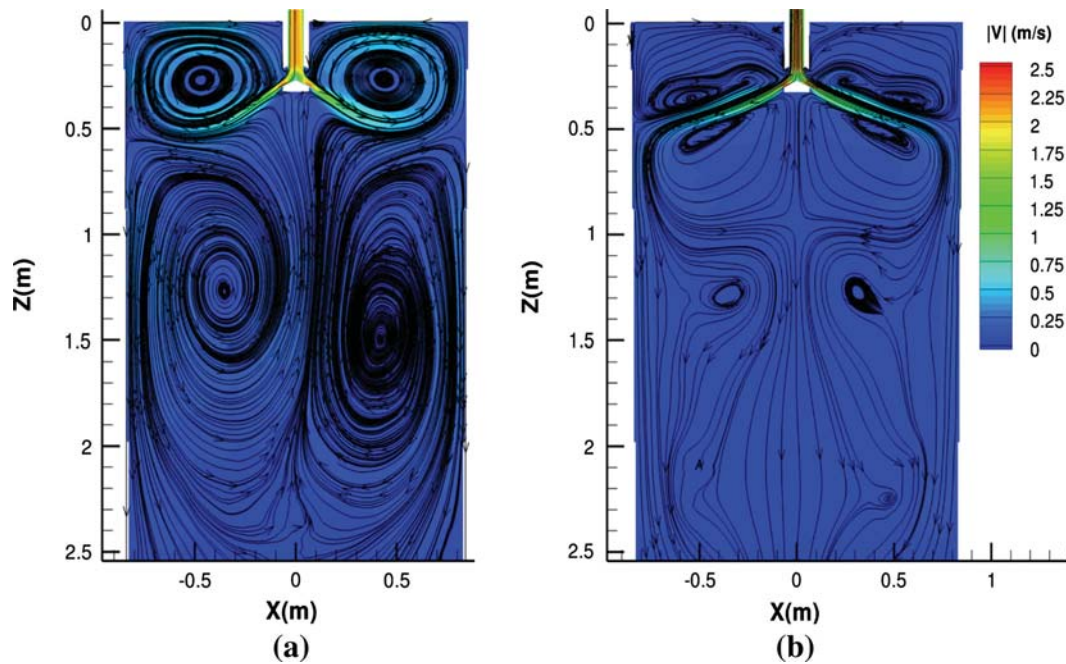


Fig. 15—Contour plot of time-averaged velocity magnitude in the mold region with streamlines (a) No-EMBr case and (b) EMBr case.

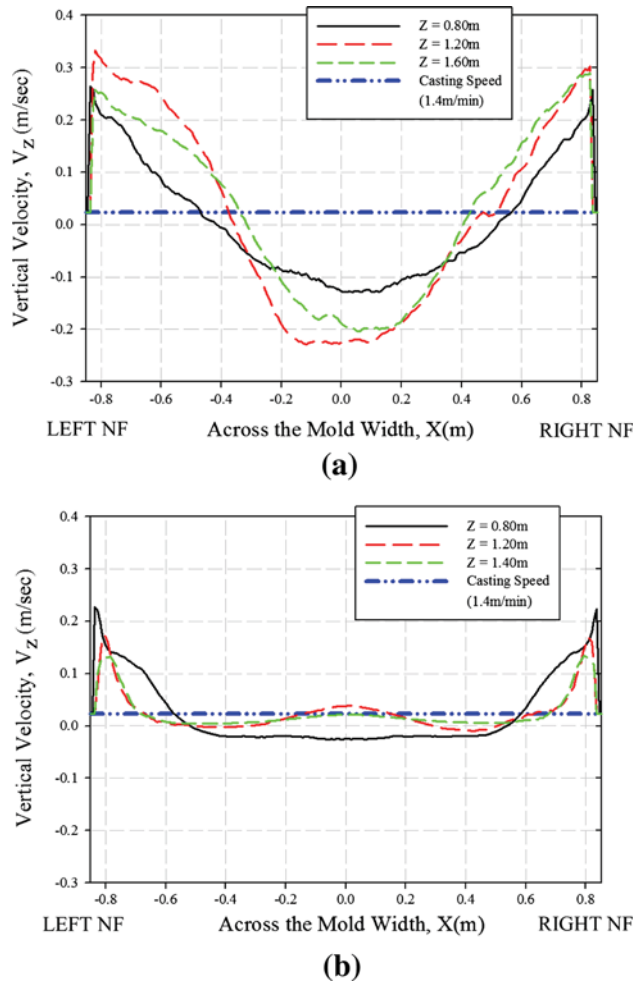


Fig. 16—Time-averaged vertical velocity (V_z) at four vertical locations in the midplane parallel to the mold WF ($Y = 0$ m) plotted across the mold width for (a) No-EMBr case and (b) EMBr case.

No-EMBr and the EMBr cases. The No-EMBr case exhibits a typical double-roll flow pattern, with the lower roll penetrating deep into the mold as mentioned earlier. The flowfield is almost symmetric after 25 seconds of averaging, with slight asymmetry in the lower roll indicating long-time transients. The flowfield is more complicated with the magnetic field. Velocities in the jet and the upper roll region are much slower. There are two small but strong recirculation zones just above and just below the jet which were observed previously.^[12] Far below the lower recirculation zones, the flow eventually tends to be downward across the entire section.

Large downward velocities below the jet region increase the penetration depth and the chances of bubbles and inclusions being captured into the solidified steel. Figures 16 and 17 show time-averaged vertical velocity profiles across the strand width at the midplane and across the strand thickness near the left NF ($X = -0.8$ m), respectively, at various vertical locations for both cases. The No-EMBr case has high downward flow near the NF, and returning flow up the center. The detrimental feature in the No-EMBr case is that the downward velocity near the NF remains high even at 1.6 m from the free surface. The EMBr case has slower downward flow near the NF, which decreases with vertical distance below the top surface.

The effect of the applied magnetic field on the turbulence can be understood by studying the time-averaged Reynolds stresses of the flow. Figure 18 shows contour plots of the normal components of the time-averaged Reynolds stresses and the TKE. Magnetic fields are known to suppress the turbulence in the flow of a conducting material,^[15] and this effect is seen here. The fluctuating components in the No-EMBr case extend along the jet, deep into the upper

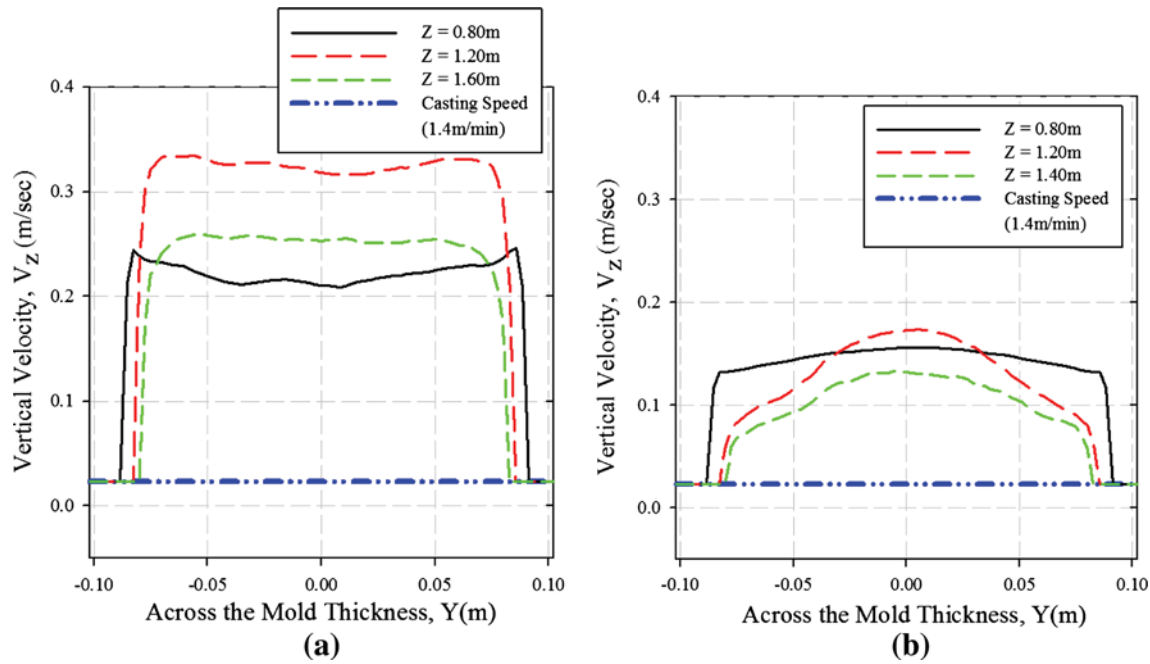


Fig. 17—Time-averaged vertical velocity (V_z) at four vertical locations in the midplane parallel to the mold WF plotted across the mold thickness at $X = -0.8$ m for (a) No-EMBr case and (b) EMBr case.

roll of the mold. In contrast, the EMBr field suppresses the turbulent fluctuations and restricts the Reynolds stresses to the jet region near the port exits, especially in the through-thickness direction of $\overline{v'v'}$. The $\overline{u'u'}$ and the TKE values are relatively high at the surface for the No-EMBr case compared with the EMBr case.

C. Surface Flow

As discussed earlier, the surface flow is critical to the steel quality. Very high surface velocities may entrain slag because of shear-layer instability,^[27] whereas very low surface velocities make the meniscus prone to freezing. Thus, the ideal surface velocity should be within a safe operating window between the upper and lower thresholds to avoid both defect mechanisms. This ideal range for top surface velocity was reported to range from 0.26 to 0.43 m/s,^[27] but the exact range should depend on the superheat, slag-layer properties, and other conditions. Figures 19(a) and (b) compare the time-averaged surface-velocity profiles across the strand width and thickness, respectively, for both cases. Across the width, the No-EMBr case has a high surface velocity with the maximum (~ 0.55 m/s) found midway between the SEN and the NF. The surface velocity with EMBr is much smaller (~ 0.1 m/s). The velocity profile across the thickness is nearly uniform. The EMBr case has a slight M-shaped profile, with maximum velocity close to the walls. This classic M-Shaped profile is observed in previous studies of MHD flow in high-aspect ratio channels through transverse magnetic fields.^[35]

Neither case has an optimal surface velocity profile within the accepted range. It is therefore recommended to tailor the magnetic field to achieve the desired surface

velocity as the No-EMBr case has other problems, such as unbalanced flow. The surface velocity with EMBr could be increased by either moving the lower ruler upward or by decreasing the strength of the upper ruler.

V. COMPARISON WITH NAIL BOARD MEASUREMENTS

The nail board measurement method is used extensively to study surface flow phenomena^[36] and has been extended^[37–39] to predict surface velocity quantitatively. This nail-dipping test produces instantaneous snapshots of the surface flowfield. Figure 20 shows a schematic of the steps in the method. An array of steel nails is dipped into the molten steel for 3 to 5 seconds, and the flow around the nail is revealed by the shape of the solidified lumps. The kinetic energy of the molten steel is converted into potential energy, which raises the steel/slag interface where the flow impacts the nail, and slopes downward in the flow direction. Rietow and Thomas^[38] performed CFD analyses of the nail-dipping test, and based on these calculations and validation measurements in a steel caster, Liu *et al.*^[39] established a correlation between the surface velocity V_{lump} (m/s) and the lump height difference Δh_{lump} (mm) as

$$V_{\text{lump}} = 0.624(d_{\text{lump}})^{-0.696}(h_{\text{lump}})^{0.567}, \quad [9]$$

where d_{lump} (mm) is the lump diameter.

The simulation with No-EMBr was performed at the same operating condition as the nail board measurements in the commercial caster, except that the 4.4 pct volume of argon gas that was injected into the SEN was not included in the model. Figure 21 shows photographs

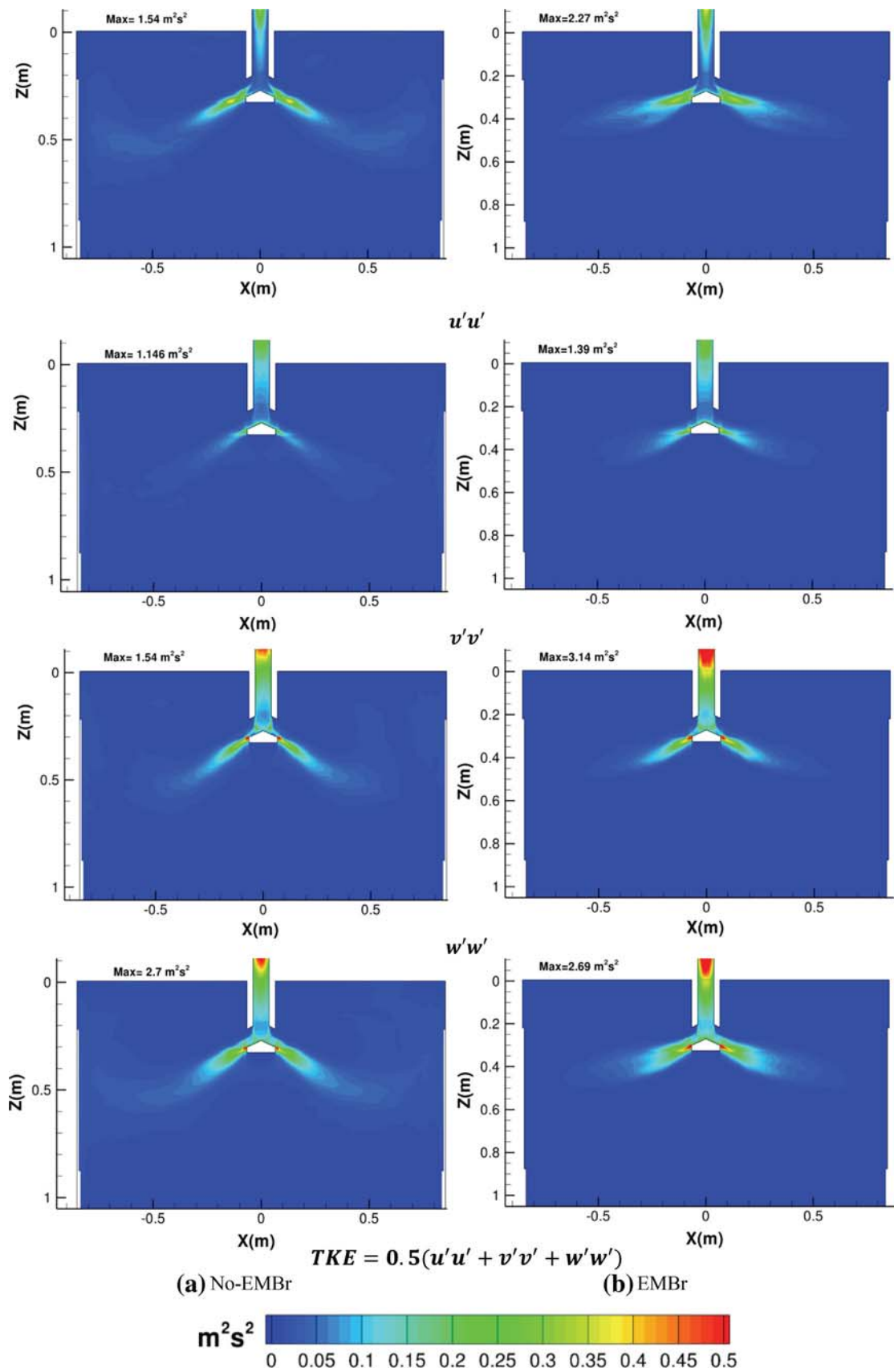


Fig. 18—Contour plots of normal components of Reynolds stresses and TKE in the mold region for (a) No-EMBr case and (b) EMBr case.

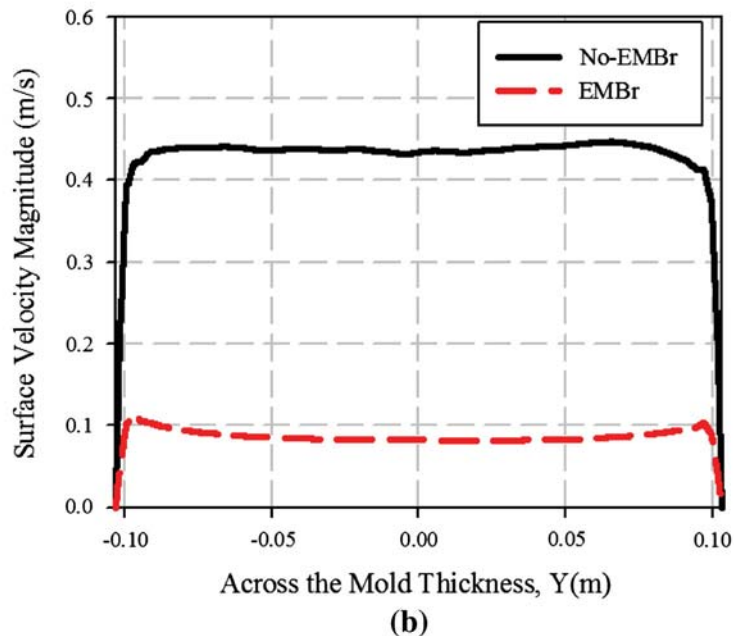
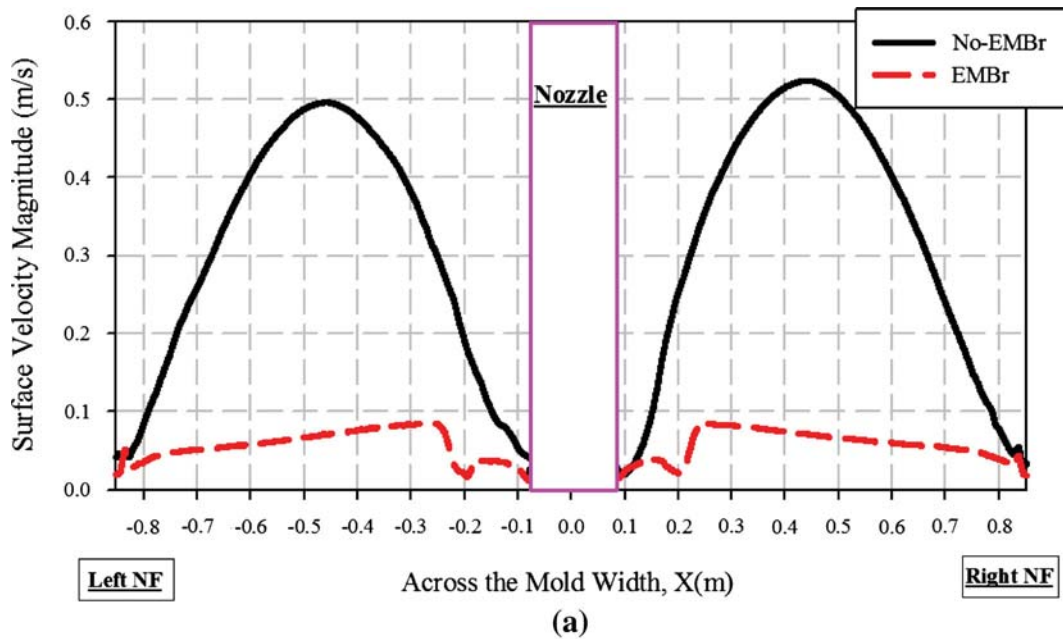


Fig. 19—Variation of time-averaged velocity magnitude (a) across the width of the mold on the top surface at $Y = 0$ mm and (b) across the thickness of the mold at $X = 0.3$ m.

of one the nail boards. There were two rows of nails, spaced ~ 50 mm apart, across the width of the mold which are referred to as the row closer to the Outer Radius (OR) or Inner Radius (IR).

Figure 22 compares the calculated surface velocity magnitudes across the mold width with the two rows of measurements based on Eq. [9]. The error bars for the measured surface velocities are obtained by performing error estimation with an assumed uncertainty of 0.5 mm in the lump height difference measurement.^[39] The measured velocities are generally higher near the NF, relative to the predictions, which show a maximum midway between the NF and SEN. This may be

explained by the unbalanced mold flow for the No-EMBr case as discussed previously. The measurements may have been taken at an instant when there was dominant recirculation in this half of the mold. To check this, an instantaneous velocity magnitude profile is included in Figure 22 at a time of higher unbalanced flow. The instantaneous profile maximum matches the measurements well, but its location is still midway between the SEN and NF. A likely explanation for this discrepancy is the neglect of argon gas effects on the calculated flow. The measured and calculated velocity vectors are compared in Figure 23. The directions generally correspond with a stable double-roll flow

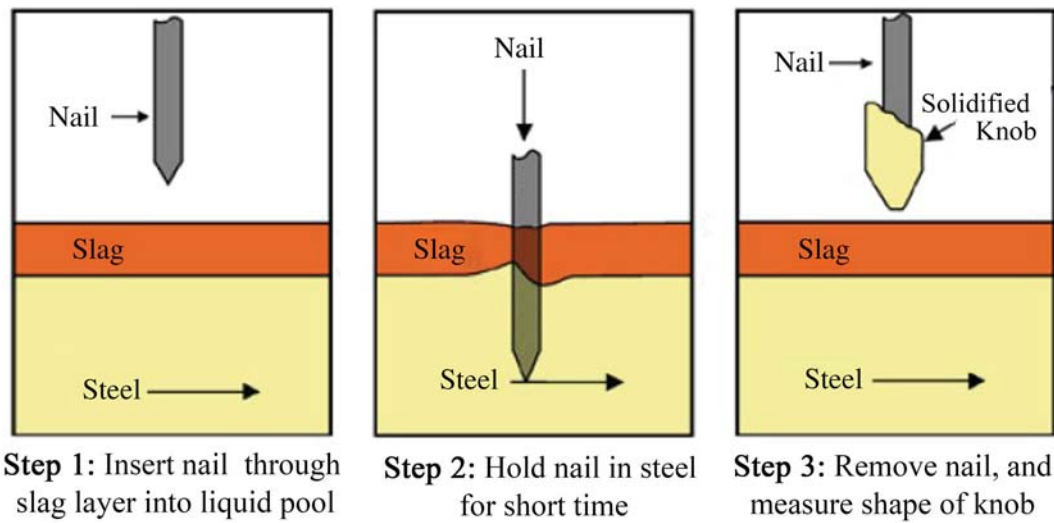


Fig. 20—Nail-board test procedure.^[1]



Fig. 21—Pictures of one of the nail boards used for the measurements at the commercial steel caster (a) front view and (b) bottom view.

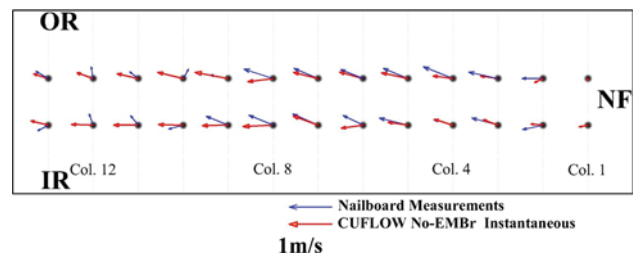


Fig. 23—Comparison of measured and calculated surface velocity vectors.

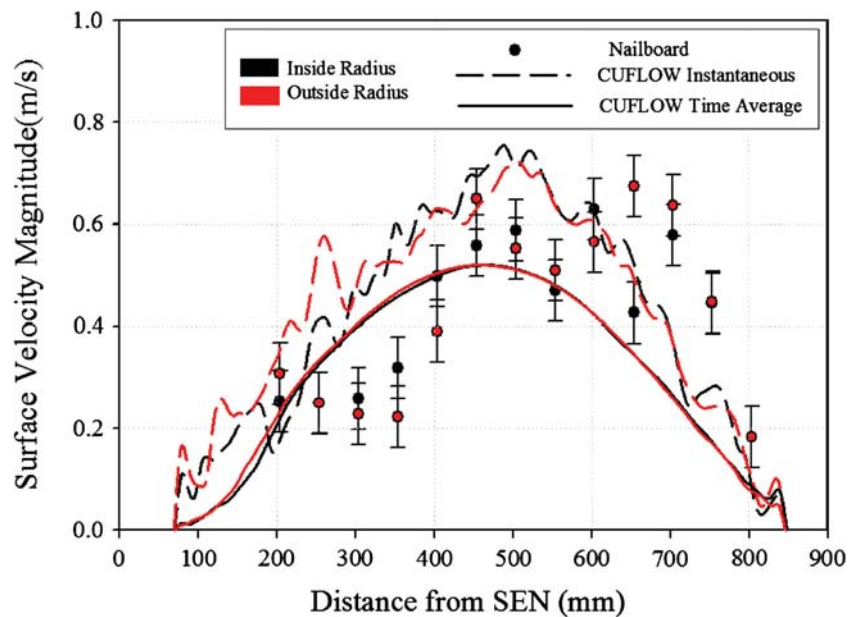


Fig. 22—Comparison of measured and calculated surface velocity magnitudes for two rows of nails on the nail board.

pattern. The observed degree of cross flow associated with velocity fluctuations also appears to match reasonably well.

The free-surface-level profile was also measured from the solidified lumps and compared with the model predictions in Figure 24. The heights of the two rows of

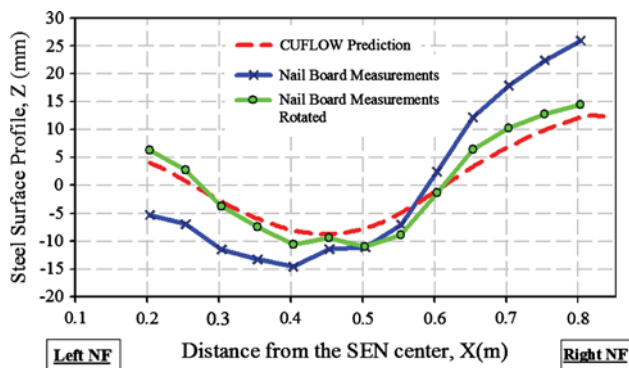


Fig. 24—Comparison of measured and calculated instantaneous surface-level profiles (rotation angle: 2.2 deg).

solidified lumps were averaged to estimate surface-level profile along the centerline. The measured and the predicted surface-level profiles match very closely if the measured profile is rotated. Pivoting about the center handle of the nail board to raise one end 10 mm and lower the other end by 10 mm could easily have been introduced while dipping the nail board manually into the mold. Even without considering this rotation, the trends of higher level on the narrow face and the lowest level midway between the SEN and NF are both predicted and measured, and these agree with a previous study.^[40] The variations of over 15 mm in height are significant.

VI. SUMMARY AND CONCLUSIONS

Large eddy simulations of a real caster at industrial operating conditions were conducted in the current study, both in the presence and in the absence of an applied magnetic field with the double-ruler or FC-Mold EMBR configuration. In the absence of EMBR, a classic double-roll flow pattern is observed with transient unbalanced flow. The upper recirculation regions have high velocities which cause large variations in the surface-level profile, (up to ~ 22 mm), large surface-level fluctuations ($\sim \pm 12$ mm), and high surface velocities (up to ~ 0.6 m/s). The lower loops penetrate deep into the strand and also have unbalanced transient behavior. A spectral analysis revealed that the unbalanced transient flow oscillations had a power peak at a time period of around 17 seconds without EMBR. This matches closely with the time period predicted by the linear relation of Honeyands *et al.*,^[28] (~ 16 seconds).

In the presence of the double-ruler magnetic field, the unbalanced flow behavior is damped, and the flow is much more stable. The jet is deflected downward, which weakens the upper recirculation regions, resulting in a flatter surface-level profile (up to ~ 1.5 mm), with extremely small level fluctuations ($< \pm 1$ mm) and lower surface velocities (~ 0.1 m/s). The magnetic field makes the flow more stable and lowers surface velocity to prevent entrainment. However, to lessen meniscus freezing problems, it might be beneficial to increase the surface flow by moving the lower ruler upward to deflect the jet

upward or by reducing the magnetic field strength of the upper ruler. The lower rolls exhibit small recirculation regions below the jet, and the flow below this region has low velocities which are mostly aligned in the casting direction. These low velocities below the jet region are beneficial in reducing the penetration depth and lowering the chances of inclusions and bubbles being entrapped in the solidifying front deep in the caster.

The calculated surface velocities for the No-EMBR case were compared with nail board measurements taken at the commercial continuous caster. It is difficult to establish a fair comparison as the measurements only provide an instantaneous snapshot of the highly transient surface flow, and the effect of argon gas was ignored in the model. However, the measured surface flow directions, velocity profile, and the free-surface-level profile all agree reasonably well with the computations.

ACKNOWLEDGMENTS

The current study was supported by the National Science Foundation Grant CMMI 11-30882, and the Continuous Casting Consortium at the University of Illinois at Urbana-Champaign. The authors are also grateful to Mr. Jonathan Powers and Mr. Thomas Henry for making the Severstal casting facility at Dearborn, MI, USA, available for the experiments and for their help during the nail board measurements. The authors further acknowledge a grant from NVIDIA for providing the Fermi GPU cards through the NVIDIA Professor Partnership program.

REFERENCES

1. K. Cukierski and B.G. Thomas: *Metall. Mater. Trans. B*, 2008, vol. 39B, pp. 94–107.
2. D. Kim, W. Kim, and K. Cho: *ISIJ Int.*, 2000, vol. 40, pp. 670–76.
3. K. Takatani, K. Nakai, N. Kasai, T. Watanabe, and H. Nakajima: *ISIJ Int.*, 1989, vol. 29, pp. 1063–68.
4. M.Y. Ha, H.G. Lee, and S.H. Seong: *J. Mater. Process. Technol.*, 2003, vol. 133, pp. 322–39.
5. H. Harada, T. Toh, T. Ishii, K. Kaneko, and E. Takeuchi: *ISIJ Int.*, 2001, vol. 41, pp. 1236–44.
6. R. Chaudhary, B.G. Thomas, and S.P. Vanka: *Metall. Mater. Trans. B*, 2012, vol. 43B, pp. 532–53.
7. B. Li, T. Okane, and T. Umeda: *Metall. Mater. Trans. B*, 2000, vol. 31B, pp. 1491–503.
8. A. Idogawa, M. Sugizawa, S. Takeuchi, K. Sorimachi, and T. Fujii: *Mater. Sci. Eng. A*, 1993, vol. 173, pp. 293–97.
9. Y. Miki and S. Takeuchi: *ISIJ Int.*, 2003, vol. 43 (10), pp. 1548–55.
10. T. Ishii, S.S. Sazhin, and M. Makhlof: *Ironmaking Steelmaking*, 1996, vol. 23, pp. 267–72.
11. Y. Hwang, P. Cha, H.-S. Nam, K.-H. Moon, and J.-K. Yoon: *ISIJ Int.*, 1997, vol. 37, pp. 659–67.
12. R. Singh, B.G. Thomas, and S.P. Vanka: *Metall. Mater. Trans. B*, 2013, vol. 44B (5), pp. 1201–21.
13. X. Miao, K. Timmel, D. Lucas, S. Ren, Z. Eckert, and G. Gerbeth: *Metall. Mater. Trans. B*, 2012, vol. 43B, pp. 954–72.
14. H. Kobayashi: *Phys. Fluids*, 2006, vol. 18, pp. 045107-1–045107-11.
15. R. Moreau: *Magnetohydrodynamics*, Kluwer, Norwell, MA, 1990, pp. 110–64.
16. R. Chaudhary, S.P. Vanka, and B.G. Thomas: *Phys. Fluids*, 2010, vol. 22, pp. 075102-1–075102-15.

17. R. Chaudhary, A.F. Shinn, S.P. Vanka, and B.G. Thomas: *Comput. Fluids*, 2011, vol. 51, pp. 100–114.
18. A.F. Shinn and S.P. Vanka: *J. Turbomach.*, 2013, vol. 135, pp. 011004-1–011004-16.
19. A.F. Shinn: PhD Thesis, University of Illinois at Urbana-Champaign, 2011.
20. R. Liu and B.G. Thomas: *AISTech 2012 Steelmaking Conference Proc.*, Atlanta, GA, May 7–10, 2012.
21. J. Iwasaki and B.G. Thomas: *Thermal-Mechanical Model Calibration with Breakout Shell Measurements in Continuous Steel Slab Casting*, Wiley, Hoboken, 2012, pp. 355–362.
22. R. Chaudhary, B.T. Rietow, and B.G. Thomas: *Materials Science and Technology*, AIST/TMS, Pittsburgh, PA, 2009, pp. 1090–101.
23. H. Werner and H. Wengle: *Proceedings of 8th Symposium on Turbulent Shear Flows*, Technical University Munich, 1991, pp. 155–68.
24. H. Bai and B.G. Thomas: *Metall. Mater. Trans. B*, 2001, vol. 32B, pp. 253–67.
25. H. Bai and B.G. Thomas: *Metall. Mater. Trans. B*, 2001, vol. 32B, pp. 269–84.
26. R. Chaudhary, G.-G. Lee, B.G. Thomas, and S.-H. Kim: *Metall. Mater. Trans. B*, 2008, vol. 39B, pp. 870–84.
27. L.C. Hibbeler and B.G. Thomas: *AISTech 2013 Steelmaking Conference Proceedings*, Pittsburgh, PA, 6–9 May 2013.
28. T.A. Honeyands and J. Herbertson: *127th ISIJ Meeting*, Tokyo, Japan, March, 1994.
29. D. Gupta and A.K. Lahiri: *Metall. Mater. Trans. B*, 1994, vol. 25B, pp. 227–33.
30. S.-M. Cho, G.-G. Lee, S.-H. Kim, R. Chaudhary, O.-D. Kwon, and B. G. Thomas: Jim Evans Honorary Symposium, in *Proceedings of the Minerals, Metals, and Materials Society 139th Annual Meeting*, pp. 71–77.
31. Q. He: *ISIJ Int.*, 1993, vol. 33 (2), pp. 343–45.
32. M. Gebhard, Q. He, and J. Herbertson: *76th Steelmaking Conference Proceedings*, The Iron and Steel Society, Warrendale, 1993, pp. 441–446.
33. J.W. Rottman: *J. Fluid Mech.*, 1982, vol. 124, pp. 283–306.
34. C. Ojeda, B.G. Thomas, J. Barco, and J. Arana: *Proceedings of AISTech*, vol. 2, The Association for Iron and Steel Technology, pp. 269–283, 2007.
35. J.C.R. Hunt: *J. Fluid Mech.*, 1965, vol. 21 (4), pp. 577–90.
36. P.H. Dauby, W.H. Emling, and R. Sobolewski: *Ironmaker Steelmaker*, 1986, vol. 13, pp. 28–36.
37. R. McDavid and B.G. Thomas: *Metall. Mater. Trans. B*, 1996, vol. 27B, pp. 672–85.
38. B. Rietow and B.G. Thomas: *AISTech 2008 Steelmaking Conference Proceedings*, Pittsburgh, PA, 5–8 May, 2008.
39. R. Liu, J. Sengupta, D. Crosbie, S. Chung, M. Trinh, and B.G. Thomas: *Sensors, Sampling, and Simulation for Process Control*, TMS Annual Meeting, San Diego, CA, Feb 27th–Mar 3rd, 2011, pp. 51–58.
40. Q. Yuan, B.G. Thomas, and S.P. Vanka: *Metall. Mater. Trans. B*, 2004, vol. 35B, pp. 685–702.